Materials and Sustainability
https://www.sciltp.com/journals/matsus

Article

Solution Deposition of High-Quality $AgBiS_2$ Thin-Films via a Binary Diamine-Dithiol Solvent System

Mehri Ghasemi [1,2,*], Dongxu He [2], Baohua Jia [1,*] and Xiaoming Wen [1,*]

[1] School of Science, RMIT University, Melbourne, VIC 3000, Australia
[2] School of Chemical Engineering, University of Queensland, Brisbane, QLD 4072, Australia
* Correspondence: mehri.ghasemi@rmit.edu.au

How To Cite: Ghasemi, M.; He, D.; Jia, B.; et al. Solution Deposition of High-Quality $AgBiS_2$ Thin-Films via a Binary Diamine-Dithiol Solvent System. *Materials and Sustainability* **2025**, *1*(2), 8. https://doi.org/10.53941/matsus.2025.100008.

Received: 18 February 2025
Revised: 8 April 2025
Accepted: 10 April 2025
Published: 21 April 2025

Abstract: Lead halide perovskites suffer from toxicity and instability challenges due to their sensitivity to various environmental factors, such as humidity, heat and prolonged light illumination. Developing stable and lead-free alternatives that can still be solution-processed has attracted significant research interests in the past years. Bismuth-based chalcogenide materials have emerged as one promising candidate. In particular, silver bismuth disulfide ($AgBiS_2$) has garnered increasing interest due to its high absorption coefficient (10^5–10^3 cm^{-1} in the 400–1100 nm range) and a favourable bandgap of ~1.3 eV. However, the poor solubility of $AgBiS_2$ precursors in the conventional solvents has hindered the solution fabrication of high-quality thin-films. While previous studies have explored deposition techniques such as spray pyrolysis, hot-injection synthesis with ligand exchange, and nanocrystal ink-based in situ passivation, these methods often involve complex ligand engineering, high processing costs, or challenges in achieving uniform and compact thin-film. In this work, we introduce a novel solution-based spin-coating approach for the deposition of high-quality, phase-pure $AgBiS_2$ thin-films, overcoming the solubility limitations of conventional precursors. By employing a binary chelating solvent mixture of ethylenediamine and 1,2-ethanedithiol, we achieve bidentate coordination with metal cations, enabling the dissolution of Ag_2S and Bi_2S_3 through a chelation-assisted mechanism. This facilitates the formation of compact and uniform films with precise roughness control. This method eliminates the need for high-temperature processing or vacuum-assisted crystallization, significantly enhancing scalability and cost-effectiveness. A planar heterojunction device architecture incorporating TiO_2 as the electron transport layer ($FTO/c\text{-}TiO_2/AgBiS_2/P3HT/Au$) is demonstrated with the initial power conversion efficiency (PCE) of 0.62%, offering an effective charge extraction pathway. With further passivation and doping optimizations, this approach presents a new, scalable route for solution-processed $AgBiS_2$ thin-films, providing a promising alternative to ligand-engineered nanocrystal-based methods with potential advantages in stability, reproducibility, and manufacturing compatibility.

Keywords: $AgBiS_2$ thin-film; chalcogenide photovoltaics; solution-processed deposition; spin-coating; binary solvent system; Pb-free solar cells

1. Introduction

Halide perovskite solar cells have emerged as a promising photovoltaic technology due to their exceptional light-harvesting capabilities, tuneable optoelectronic properties, and high power conversion efficiencies [1–3].

Copyright: © 2025 by the authors. This is an open access article under the terms and conditions of the Creative Commons Attribution (CC BY) license (https://creativecommons.org/licenses/by/4.0/).
Publisher's Note: Scilight stays neutral with regard to jurisdictional claims in published maps and institutional affiliations.

This is contributed to the remarkable features of this class of materials such as direct narrow bandgap of 1.6 eV [4] that is very close to the optimum Schockley-Queisser value for single-junction solar cells (1.43 eV), high absorption coefficient of 5×10^4 cm^{-1} in red wavelengths [5], long electron and hole diffusion lengths of 1 μm [6–8] along with their small and balanced electron and hole effective masses [6,9]. These superb optoelectronic characteristics are more exciting when the easy film preparation of these materials via inexpensive solution-processed routs is also acknowledged [10]. These outstanding features have propelled the employment of perovskites in other optoelectronic applications such as semiconductor lasers [11] and light-emitting diodes [12].

As halide perovskite solar cells have rapidly approached their theoretical efficiency limits within just a few years, a critical question arises: what hinders the transition from laboratory-scale research to large-scale commercialization? One of the primary challenges is the intrinsic instability of perovskite materials, as they are highly susceptible to humidity, heat, and prolonged illumination. However, significant progress has been made in enhancing stability through compositional engineering strategies, including cation tuning, halide mixing, and additive incorporation, which have mitigated degradation to an acceptable extent [13,14]. Beyond stability concerns, the most pressing limitation remains toxicity, due to the presence of lead (Pb) in the perovskite structure [15–17]. This raises serious concerns regarding the environmental and health impacts of lead emissions throughout the material's life cycle [18,19]. A potential solution is the replacement of Pb with alternative elements, such as tin (Sn) [20–23], copper (Cu) [24–26], bismuth (Bi) [27–32], antimony (Sb) [33–36], or germanium (Ge) [37–39]. However, despite extensive efforts, none of these candidates have been able to match the exceptional light-absorbing and electronic properties of Pb-based perovskites. Consequently, it appears that lead plays a crucial role in achieving high photovoltaic performance. This suggests that a more effective approach may be to explore alternative, non-toxic material systems beyond the perovskite framework.

Among the promising alternatives, chalcogenide materials have attracted attention due to their tunable and favorable catalytic, thermoelectric, and optoelectronic properties, making them highly applicable in energy storage [40,41], electrocatalysis [42,43], non-linear optics [44], and photovoltaics [41,45]. Traditionally, chalcogenides employed in these applications have been binary metal compounds, often based on toxic or rare elements such as tellurium, cadmium, and indium [46–48]. Given the high cost and environmental concerns associated with these materials, recent research has shifted toward developing less toxic and earth-abundant alternatives [49]. In this regard, ternary chalcogenides, composed of non-toxic, cost-effective elements, have emerged as an attractive solution [50,51]. Among these, silver bismuth disulfide ($AgBiS_2$) stands out as a highly promising candidate for photovoltaic applications, owing to its exceptional optoelectronic properties, including a high absorption coefficient (10^5–10^3 cm^{-1} in the 400–1100 nm range) [51,52], a stable cubic phase at 200 °C, stoichiometric stability [53], and a narrow bandgap of approximately 1.3 eV [51], Its potential as a solar absorber has been demonstrated in thin-film photovoltaic devices, where Bernechea et al. reported a power conversion efficiency (PCE) of 6.3% for ultra-thin (~35 nm) absorber layers [54], More recently, Oh et al. introduced a post-deposition in situ passivation strategy for $AgBiS_2$ nanocrystal inks, significantly enhancing film morphology, trap-state density reduction, and charge carrier dynamics [55]. This approach, leveraging a multifunctional molecular agent for colloidal dispersibility and surface passivation, enabled the fabrication of ultrathin, defect-free films, achieving a record PCE exceeding 10%. Despite these advancements, the challenge of developing scalable and cost-effective deposition methods for producing compact, uniform $AgBiS_2$ thin-films persists. To address this, the development of a feasible, highly reproducible, and cost-effective deposition strategy is critical to enable the integration of $AgBiS_2$ into photovoltaic devices. Spin-coating is among the most favourable thin-film deposition techniques, offering simplicity, versatility, reproducibility, and scalability. Previous studies have reported the fabrication of $AgBiS_2$ thin-films via spin-coating, primarily through chemically synthesized nanoinks [56] or other solution-based approaches [57]. However, these methods often rely on multi-step ligand-exchange processes, complex nanocrystal synthesis, or post-deposition modifications, which can limit scalability and reproducibility.

In this work, we present a direct solution-processed spin-coating approach for $AgBiS_2$ thin-film fabrication. This method allows for precise control over film thickness by varying the solution concentration and, more importantly, eliminates the need for high-temperature processing or sophisticated vacuum systems to control crystallization. To overcome precursor solubility limitations, we introduce a binary solvent system composed of ethylenediamine and 1,2-ethanedithiol, which effectively dissolves Ag_2S and Bi_2S_3 precursors, facilitating the formation of high-quality thin-films. Furthermore, this scalable and cost-effective deposition strategy enables the fabrication of compact, uniform, and phase-pure $AgBiS_2$ films, making it suitable for photovoltaic applications. A planar heterojunction device architecture incorporating c-TiO_2 as the electron transport layer (FTO/c-TiO_2/$AgBiS_2$/P3HT/Au) is demonstrated, achieving an initial PCE of 0.62%, highlighting the feasibility of this approach. With further passivation and doping optimizations, this method offers a new pathway for solution-processed $AgBiS_2$ photovoltaics, providing advantages in stability, reproducibility, and large-scale manufacturing compatibility.

2. Materials and Methods

All steps of materials deposition and device fabrication were performed in glovebox except compact TiO_2 spray pyrolysis step.

FTO glass slides (FTO22-7, Yingkou OPV Tech New Energy Co. Ltd. Yingkou, China) were cleaned sequentially by ultra-sonicating in acetone, ethanol, and isopropanol for 20 min. Then dried in the oven at 70 °C for 20 min for drying. Finally, the surface was cleaned using UV-Ozone for 20 min. Afterwards, a 0.42 M precursor solution of titanium diisopropoxidebis (acetylacetonate) (75 wt.% in isopropanol) was prepared in anhydrous 2-propanol then using spray pyrolysis method was deposited on the cleaned FTO substrate to prepare a properly compact TiO_2 layer (c-TiO_2) was used to deposit a thin compact-TiO_2 (c-TiO_2) layer by spray pyrolysis. Deposited TiO_2 layer was annealed at 530 °C for 20 min. Before depositing $AgBiS_2$ layer, c-TiO_2 layer covered FTO was treated with UV Ozone for 15 min. Finally, $AgBiS_2$ thin-film deposited as explained in the previous part (en:edtH_2 5:1, 4:1, 3:1, Ag_2S:Bi_2S_3 molar ratio 1:0.8, 1:1, 1:1.2, 1:1.5, at 3000 RPM and the annealing temperature of 180 °C).The hole transport layer (HTL) was prepared by spin-coating pristine poly(3-hexylthiophene-2,5-diyl) (P3HT) (Sigma-Aldrich, St. Louis, MO, USA, Mw 54,000–75,000, 15 $mg\cdot ml^{-1}$ in 1,2-dichlorobenzene) solution at 2000 rpm for 30 s at 1000 $rpms^{-1}$. In order to dry the layer and remove the additional solvent, an annealing step at 100 °C for 15 min was effective for solvent removal. Finally, ~50 nm Au was thermally deposited as the contact electrode by a thermal evaporator (DD ONG high technology, Shenzhen, China). The measure aperture area was 0.08 cm^2.

Characterizations and Measurements: For characterizations, powder X-ray diffraction measurement was performed on a Bruker Advanced X-ray Diffractometer with Cu Kα radiation from 10° to 50° (2θ). A field-Emission Scanning Electron Microscope (FE-SEM, JEOL 7100, Tokyo, Japan) recorded scanning electron microscope (SEM) images of the sample morphologies. Absorption spectra of the films were performed on a UV-visible light spectrometer (Shimadzu UV2450, Kyoto, Japan). Kratos Axis Supra Photoelectron Spectroscopy was used for ultraviolet photoelectron spectroscopy (UPS) measurement. A solar simulator (AM 1.5, 100 $mW\cdot cm^{-2}$, Oriel, Stratford, CT, USA) equipped with a Keithley 2420 digital source meter was used to record current-voltage (I–V) plots. A Newport 1918-c power meter equipped with a 300 W Oriel xenon light source and an Oriel Cornerstone 260¼ m monochromator in a DC mode was used to measure the incident photon-to-current conversion efficiency (IPCE). A standard Si reference was used before the IPCE measurement. XPS with Al Kα ($h\nu = 1253.6$ eV) radiation source was used to characterize the chemical composition of the samples and C 1 s (284.8 eV) was used to calibrate binding energies. Fourier-transform infrared (FTIR) spectroscopy was performed using a Bruker Alpha II spectrometer in attenuated total reflectance (ATR) mode. Spectra were collected in the mid-IR range of 1000 to 1800 cm^{-1} with a resolution of 4 cm^{-1}, averaging 32 scans per sample. The analyzed samples included pure ethylenediamine (en), pure 1,2-ethanedithiol (edtH_2), Ag_2S + Bi_2S_3 dispersed in en, and Ag_2S + Bi_2S_3 in the en:edtH_2 binary solvent system (4:1 *v*/*v*). Each liquid sample (~20 μL) was applied directly onto the ATR crystal under a dry N_2 atmosphere to reduce ambient moisture effects. Baseline correction was applied to all spectra. Peak positions and relative shifts in the 1150–1300 cm^{-1} region were analyzed to assess coordination between the solvent ligands and metal cations, with particular focus on C-N stretching in en and C-S/CH_2 modes in edtH_2. Film thickness was measured using a surface profilometer (Dektak-style or similar) by scanning across a scratched region on the coated substrate to determine step height.

For the stability test, $AgBiS_2$ thin-films deposited on the glass substrates were placed in the ambient air with an average humidity of 61 ± 5% for 53 days, XRD spectra of the films were recorded on the first, 9th and 20th, 30th, 42th and 53th day to check the degradation behavior.

3. Results

Developing a solution-processed thin-film deposition approach for semiconductors facilitates the employment of these materials for various applications of non-linear optics [58], transistors [59,60], photovoltaics [61,62] and memory devices [63,64]. By virtue of the liquid inks prepared in this method, an authentically homogenous film by controlling deposition parameters can be produced [65]. Unfortunately, despite the promising properties of metal chalcogenides, they are mainly insoluble in the most well-known solvents. There are some reports on the solubility of (K,Rb,Cs)-$ZrPS_6$, (K,Rb)PSe_6 in N,N-dimethylformamide [66], As_2S_3 in Amine based solvents [67], (Li,Na)$AsSe_2$ in methanol [68] and some other components such as In_2Se_3, Cu_2S, etc. in hydrazine [69,70]. However, the dissolution of a great number of metal chalcogenides specifically $AgBiS_2$ is still challenging.

Although hydrazine has been able to prove its dissolution capability, the function of this solvent is suppressed by its carcinogenic and toxic nature. In terms of colloidal dispersed-nanocrystals inks introduced for working with this group of materials, there are some serious challenges for scaling up [71]. Hence, Webber et al. made some efforts to examine the solubility of nine bulk V_2VI_3 semiconductors (V = As, Sb, Bi; VI = S, Se, Te) in a binary solvent mixture comprised of 1,2-ethylenediamine (en) and 1,2-ethanedithiol (edtH_2), which explains adding some small amount of edtH_2 is beneficial for promoting the dissolution of precursors at room temperature [65]. The enhanced solubility of V_2VI_3 chalcogenides in the binary solvent mixture of 1,2-ethylenediamine (en) and 1,2-ethanedithiol (edtH_2) is attributed to a combination of chelation, ionization, and hydrogen bonding effects. The bidentate nature of both en and edtH_2 facilitates strong coordination with metal cations, while the formation of thiolatochalcogenometallate anions increases the overall ion concentration, improving dissolution. Additionally, the significant rise in electrolytic conductivity upon mixing en and edtH_2 suggests the formation of an ionic solvent system, further stabilizing the dissolved species. This approach has been demonstrated for Bi_2S_3 and Sb_2Se_3, and a similar mechanism is expected to enhance the solubility of Ag_2S and Bi_2S_3, enabling the preparation of high-quality $AgBiS_2$ thin-films from solution processing. Inspired by this work, we attempted to examine the solubility of a mixture of Ag_2S and Bi_2S_3 as the constituent ingredients of $AgBiS_2$. The detailed dissolution process of these precursors and thin-film deposition from the prepared solutions to obtain high-quality $AgBiS_2$ thin-film is discussed in this section. At the first step, solubility of Ag_2S and Bi_2S_3 in en:edtH_2 with volume ratio of 10:1 in air with humidity of 65% was examined. As can be seen from Figure S1a, it is obvious that the adopted solvents have reasonable ability to dissolve the raw materials; however, still some black powder at the bottom of vial is obvious. Regarding film quality, even by using different deposition speed, film could not address an acceptable quality (Figure S1b). According to the colour change in the solution exposed to air, it can be concluded that the reason of this low quality should be related to the detrimental effect of humidity on the precursor solution and the ultimate thin-film (Figure S1c). Therefore, in the next step film deposition process was transferred into the glovebox with inert atmosphere of N_2 gas, which confirmed the damaging effect of humidity on both solution and thin-film (Figure S2a,b). With the aim of increasing thin-film quality some optimization steps were taken to evaluate the influence of different parameters on film quality. The first examined parameter was en:edtH_2 volume ratio. From Figure S3a–d it is clear that en:edtH_2 volume ratio has a significant impact on solution viscosity, as by increasing edtH_2 amount viscosity of the solution significantly increases, as far as for solution with en:edtH_2 volume ratio of 2:1 the solution could not be filtered and consequently no thin-film could be obtained for this solution (Figure S3a). In terms of the $AgBiS_2$ thin-films, increasing edtH_2 into the precursor solution showed its remarkable effect on the thin-film coverage. Such that the solution with highest viscosity (en:edtH_2 volume ratio of 3:1) could not properly spread during spin coating, which leaded to some obvious pinholes on the thin-film (Figure S3b). However, slightly decreasing edtH_2 into the precursor solution, by adopting en:edtH_2 volume ratio of 4:1 and 5:1, thin-films with better coverage could be brought forth. This highlights the notable impact of edtH_2 amount into the solution on the final thin-film quality; and the optimized en:edtH_2 volume ratio should be close to 4:1. To reach a better understanding on this, SEM characterization was employed to accurately evaluate thin-films quality. As seen in Figure 1a–c, by decreasing en:edtH_2 volume ratio thin-films exhibit a degradation in coverage quality, which is quite significant for film prepared from solution with en:edtH_2 volume ratio of 3:1 (Figure 1c). While for other adopted ratios of 5:1 and 4:1 better coverage on the substrate was observed (Figure 1a,b). A possible reason of this observation should be contributed to the chemical structure of edtH_2. In general, edtH_2 with a chemical formula of $C_2H_6S_2$ contains some sulphide that is likely to react with the precursor materials in the precursor solution and finally shows its contribution to the solution viscosity and thin-film coverage. Regarding to this, in a quick try some sulfur powder was externally added to the solution considering the molar ratio of 1:1:0.5 between Ag_2S:Bi_2S_3:S. However, no promising improvement in film quality could gain using this method (Figure S4a–c). In another attempt, to understand sulfur influence on film quality, different ratios for the constituent ingredients of Ag_2S and Bi_2S_3 was investigated while en:edtH_2 volume ratio was kept at a constant amount of 4:1. Interestingly, it was observed that different molar ratios of Ag_2S:Bi_2S_3 in the precursor solution also has a significant effect on viscosity of the obtained solutions, as by increasing Bi_2S_3 amount viscosity increases (Figure S5a–d). A more important point of this evaluation was the influence of these different ratios on the film character, so long as the solution contains a higher amount of Bi_2S_3 (decreasing Ag_2S:Bi_2S_3 molar ratio) outstanding thin-film with an excellent coverage was prepared. $AgBiS_2$ thin-film with a mirror-like appearance was obtained for the condition of Ag_2S:Bi_2S_3 molar ratio of 1:1.5 (Figure S5d).

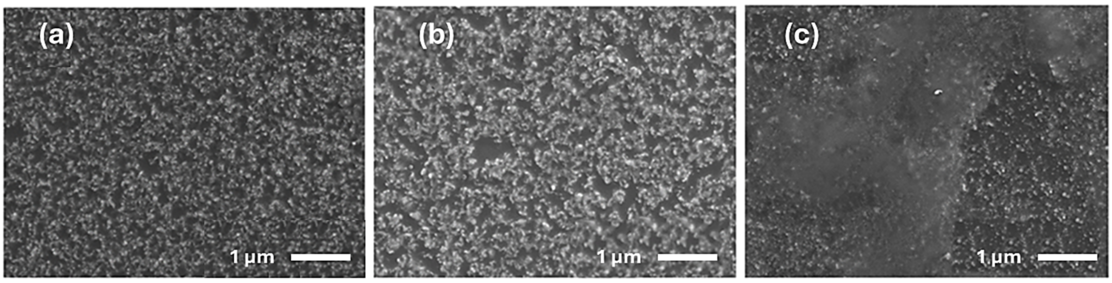

Figure 1. SEM images of the $AgBiS_2$ thin-films with different en:edtH_2 volume ratio of (**a**) 5:1, (**b**) 4:1, (**c**) 3:1.

SEM characterization of the above thin-films opens more about the morphological structure of the thin-films with different Ag_2S:Bi_2S_3 molar ratio. From the SEM images (Figure 2a–c), it can be seen that for high ratio of Ag_2S:Bi_2S_3 (1:0.8 and 1:1) film contains large-size grains poorly connected to each other with numerous pin-holes in between (Figure 2a,b), while by decreasing this ratio (1:1.2 and 1:5) grain size gradually decreases, which leads to better connection between the grains and declining number and size of the pin-holes (Figure 2c,d). Smooth $AgBiS_2$ thin-film is obtained by using Ag_2S:Bi_2S_3 molar ratio of 1:1.5, which means a higher amount of Bi_2S_3 into the precursor solution has a synergistic effect. At this condition, film is established by small-sized grains with outstanding compactness in compare to the ones with fewer Bi_2S_3 (Figure 2d). From this observation, it can be concluded that Ag_2S:Bi_2S_3 molar ratio is much more effective than en:edtH_2 ratio to produce highly dense and greatly reflective $AgBiS_2$ thin-film. In addition to improved coverage and surface morphology, variations in precursor composition were also found to influence the overall film thickness. As the Bi_2S_3 content increased, a gradual thickening of the deposited film was observed, with estimated values ranging from approximately 180 nm at a 1:0.8 molar ratio to ~255 nm at 1:1.5. This trend is consistent with the enhanced surface uniformity and reduced roughness seen in SEM and AFM analyses, suggesting that a higher Bi_2S_3 content facilitates more complete and uniform precursor deposition during spin coating.

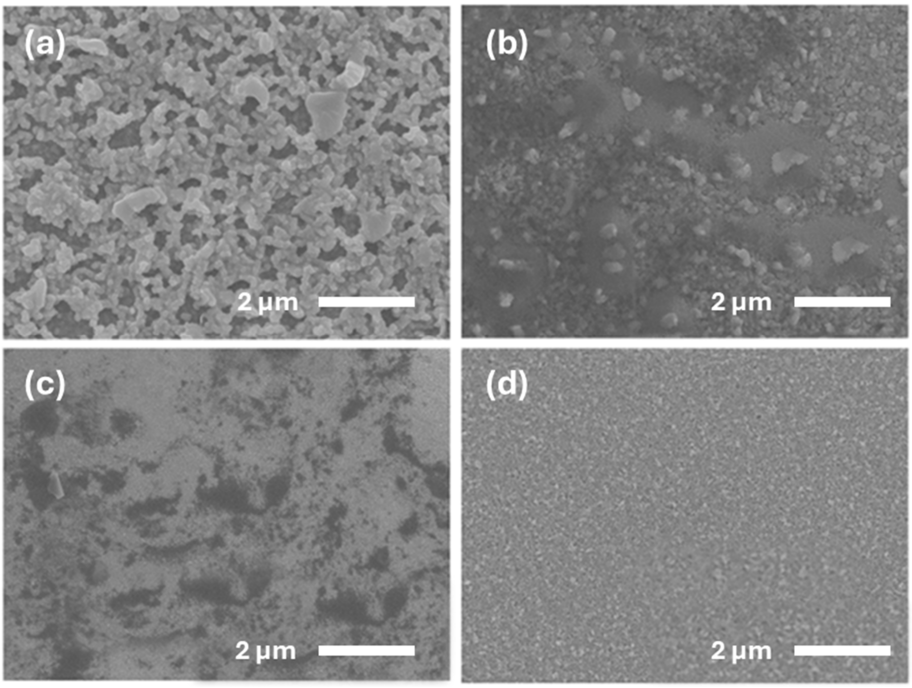

Figure 2. SEM images of $AgBiS_2$ thin-films with different Ag_2S:Bi_2S_3 ratio of (**a**) 1:0.8, (**b**) 1:1, (**c**) 1:1.2, (**d**) 1:1.5.

It has been demonstrated that better surface coverage of the active layer can attain higher photocurrent [40]. Low coverage characteristic of a particular thin-film increases surfaces roughness and number of pinholes in the film which leads to an inefficient light-absorbing ability. Whereas a compelling light-absorbing should have a smooth surface in order to adjust a successful charge transport layer deposition, forming a perfect interface for charge transportation and lowering the chance of charge recombination by suppressing the direct contact between HTL and ETL. Regarding these facts, the surface roughness of the films with different Ag_2S:Bi_2S_3 molar ratio was investigated by atomic force microscopy (AFM), represented in Figure 3a–h. Benchmark film with Ag_2S:Bi_2S_3 molar ratio of 1:0.8 showed a root-mean-square roughness (RMS) of approximately 30.71 ± 0.15 nm, while gradually increasing Bi_2S_3 from 1 mole to 1.2 moles and 1.5 moles into the precursor solution reduced this term to lower values of 25.91 ± 0.19, 20.57 ± 0.12 and 17.31 ± 0.18 nm respectively. This momentous reduction in surface roughness can be a reasonable hypothesis that a higher molar ratio between Ag_2S and Bi_2S_3 into the precursor solution has a tangible influence on the morphological properties of the film. Although a direct SEM image corresponding to the sample in Figure 3e,f is not available, the observed trend in surface roughness reduction is in strong agreement with the morphological changes shown in the SEM images in Figure 2. These consistent trends between SEM and AFM support the influence of Bi_2S_3 content on grain refinement and film uniformity.

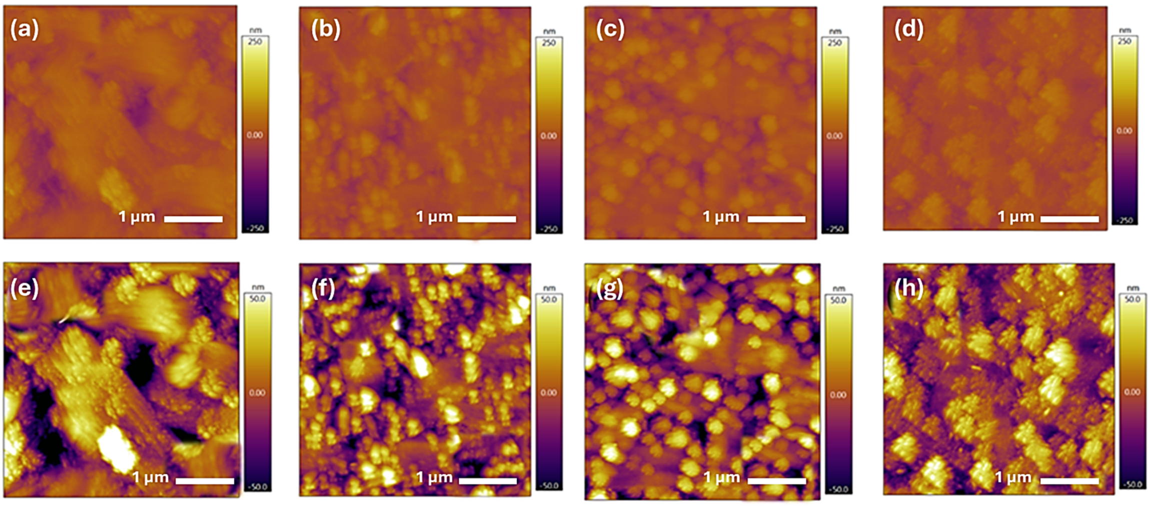

Figure 3. Topography images of $AgBiS_2$ films on FTO substrate with different Ag_2S:Bi_2S_3 molar ratio of (**a**,**b**) 1:0.8, (**c**,**d**) 1:1, (**e**,**f**) 1:1.2, (**g**,**h**) 1:1.5.

Using powder X-ray diffraction (XRD), a systematic investigation on the influence of annealing temperature on the phase formation of $AgBiS_2$ thin-films was undertaken, based on an Ag_2S:Bi_2S_3 molar ratio of 1:1 following the literature. From Figure 4a, it can be seen that an annealing temperature of 160 °C is roughly sufficient for initiating the formation of cubic-phase $AgBiS_2$, as the main characteristic peaks corresponding to the (111), (200), and (220) planes are clearly recognisable in the spectrum. However, the presence of additional peaks around 38° and 39° suggests incomplete conversion, with residual secondary phases. Slightly increasing the annealing temperature enhances crystallinity and phase purity, as reflected by the sharpening of $AgBiS_2$ peaks and the gradual suppression of unwanted reflections. At 210 °C, the diffraction pattern exhibits strong orientation along the (111) and (200) directions, with improved peak intensity and a notable reduction in impurity features, indicating high-purity $AgBiS_2$ film formation. The inclusion of a reference pattern for cubic-phase $AgBiS_2$ in Figure 4a further supports this structural identification and allows direct comparison with the experimental spectra. It is worth mentioning that all the SEM images presented above were acquired for the film annealed at 210 °C. Since the Ag_2S:Bi_2S_3 molar ratio was found to significantly affect film quality, further experiments were conducted to examine its impact on crystallinity while fixing the annealing temperature at 180 °C. The corresponding XRD patterns (Figure 4b) demonstrate a clear dependence of phase formation on precursor composition. At a molar ratio of 1:0.8, the thin-film exhibits extra peaks around 38° and 39°, similar to the trend observed at lower annealing temperatures (Figure 4a), indicating incomplete crystallisation. However, as the Bi_2S_3 content is increased (Ag_2S:Bi_2S_3 ratio adjusted from 1:1 to 1:1.5), the diffraction peaks become sharper and better aligned with the reference pattern, with diminished impurity features and stronger reflections from the (111) and (200) planes. This evolution confirms that careful tuning of precursor composition enables high-quality cubic-phase $AgBiS_2$ formation, even at reduced annealing temperatures. The film produced under optimal conditions (1:1.5 molar ratio at 180 °C) displays uniform coverage and a mirror-like surface (Figure S6a), similar to the morphology observed at 210 °C (Figure 2d). Thermal gravimetric analysis (TGA) further confirms the excellent thermal stability of the as-deposited $AgBiS_2$ thin-film, retaining integrity up to approximately 700 °C (Figure S6b).

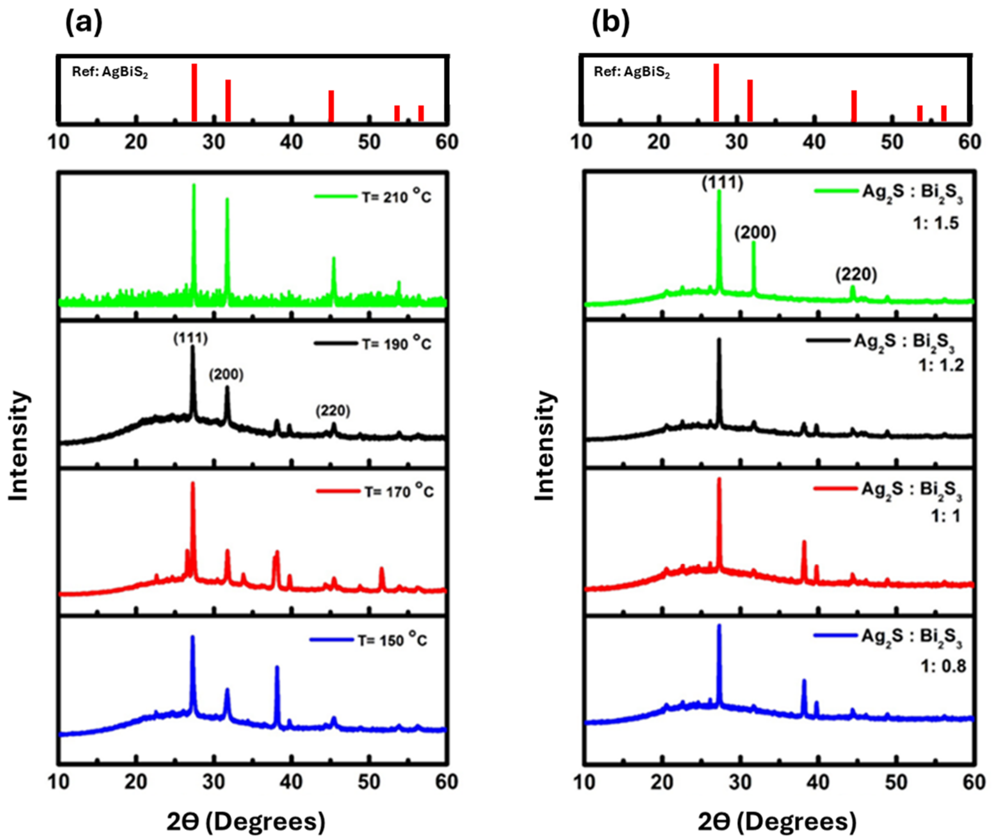

Figure 4. XRD pattern of $AgBiS_2$ thin-films (**a**) annealed at different temperatures, (**b**) Using different Ag_2S:Bi_2S_3 molar ratio.

Energy dispersive Xray spectroscopy (EDS) characterization also was used to more deeply investigate the influence of the Ag_2S:Bi_2S_3 molar ratio on the elemental composition of the final films. EDS characterization shows the intense influence of Ag_2S:Bi_2S_3 molar ratio on the degree of compositional agreement. Practically, in $AgBiS_2$ thin-film with high purity that has been crystallized in the right phase the theoretical stoichiometric ratio between Ag:Bi:S elements should be 1:1:2. From Figure S7 and the atomic percentage description in Table 1, it is obvious that in thin-films with lower amount of Bi_2S_3 (Ag_2S:Bi_2S_3 molar ratio of 1:0.8 and 1:1) in precursor solution the atomic ratio much deviates from the theoretical one, which demonstrate the incomplete transformation of film to the cubic phase. On the other hand, for films with a higher Bi_2S_3 component, this trend is less noticed (Ag_2S:Bi_2S_3 molar ratio of 1:1.2). Finally for the film with Ag_2S:Bi_2S_3 molar ratio of 1:1.5 a reasonable agreement between the detected elements' ratio and the expected stoichiometric one is obtained. This observation, consistent with the XRD results, emphasises on the critical role of raw ingredients molar ratio into the precursor solution to satisfy film crystallization into the right phase and its morphology.

Table 1. EDS elemental composition of $AgBiS_2$ thin-films with different Ag_2S:Bi_2S_3 molar ratio annealed at 180 °C.

Ag2S:Bi_2S_3 Molar Ratio	Ag Atom%	Bi Atom%	S Atom%
1.0:0.8	33.27	7.89	58.84
1.0:1.0	18.22	9.64	72.14
1.0:1.2	34.10	27.63	38.27
1.0:1.5	20.71	20.85	58.44

X-ray photoelectron spectroscopy (XPS) was employed to examine the surface composition of $AgBiS_2$ film with Ag_2S:Bi_2S_3 molar ratio of 1:1.5. The detected elements were Bi, Ag, carbon (C) and oxygen (O) (Figure 5a,b). The presence of the latter two is not unusual, because detecting a C-O functional group on the surface of the XPS sample is very common. The measured binding energies value for Ag $3d_{5/2}$, S $2p_3/_2$ from their high-resolution scan are determined to be at 367.6 eV (Figure 5c) and 161.9 eV (Figure 5d) respectively, which are consistent with those reported for Ag_2S in the literature, where values of ~367.6 eV and ~161.8–162.0 eV have been observed for silver and sulfur, respectively [72–74]. Regarding Bi $4f_{7/2}$ peak, from the high-resolution scan of Bi (Figure 5d) binding energy at 158.62 eV is detected, which is close to the reported value for Bi_2S_3 (158.8 eV) rather than the one for elemental Bi (156.9 eV).

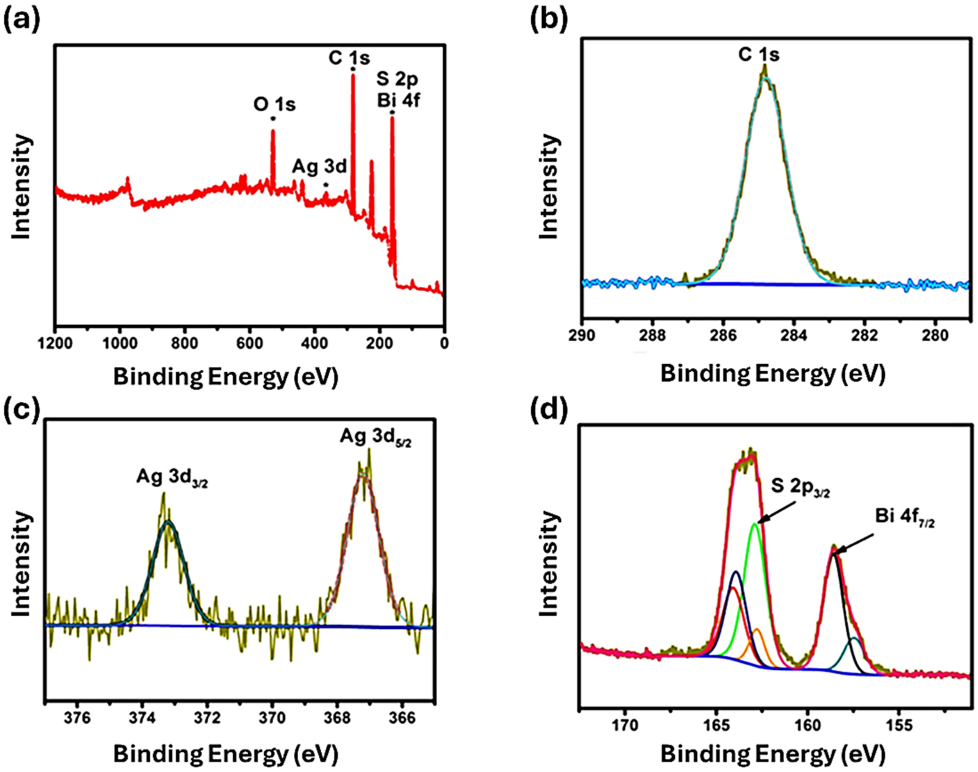

Figure 5. XPS spectra of $AgBiS_2$ thin-film with Ag_2S:Bi_2S_3 molar ratio of 1:1.5 and annealed at 180 °C, (**a**) Survey graph, (**b**) C 1s high resolution graph, (**c**) Ag 3d high resolution graph, (**d**) S 2p and Bi 4f high resolution graph. The colored lines represent fitted peaks, while the blue lines indicate the background used in the fitting.

Optical properties of $AgBiS_2$ thin-films with different precursor's molar ratio were characterized employing UV-vis spectroscopy. In this part also the impact of using different Ag_2S:Bi_2S_3 molar ratio on absorption and the bandgap characteristics of the thin-films was examined. Similar to the crystallization behaviour of the product, varying precursors molar ratio shows an obvious effect on absorption ability of the thin-films, such that increasing this molar ratio absorption intensity of the films continuously increases (Figure 6a). The reason for this behaviour should be related to better coverage of the film on the substrate. Evaluating Tauc plot of the thin-films, direct bandgap transitions of 1.46 eV, 1.45 eV, 1.44 eV and 1.44 eV are calculated respectively for thin-films with Ag_2S:Bi_2S_3 molar ratios of 1:0.8, 1:1, 1:1.2 and 1:1.5, which are all in a very close range (Figure 6b). That means the influence of changing raw materials molar ratio on this optical characteristic is not highly sensitive and it mainly shows its affection on absorption ability. Comparing these calculated bandgaps to the ones reported in the literature (1.3 [54] and 1.25 [75]), it can be seen that $AgBiS_2$ thin-film prepared by solution-processed method has slightly wider bandgap value.

While the optimized Ag_2S:Bi_2S_3 ratio and en:edtH_2 solvent balance produced compact, crystalline films, the unusual effectiveness of this binary solvent system in dissolving both metal sulfides warranted closer investigation. Unlike most chalcogenide precursors, Ag_2S and Bi_2S_3 exhibit inherently low solubility in common organic solvents due to their strong ionic lattice and limited donor–acceptor interactions. However, the en:edtH_2 system enables clear, stable solutions under ambient conditions. This observation, along with the high ionic conductivity of the precursor solution, suggested that the dissolution process may involve coordination between the solvent molecules and metal cations, facilitating the breakdown of the sulfide lattice [65]. To explore this hypothesis, we performed FTIR spectroscopy on neat en, edtH_2, and their mixtures with Ag_2S and Bi_2S_3 precursors. As shown in Figure 6, the spectra collected in the 1000–1800 cm^{-1} region exhibit clear changes in vibrational features. a dominant peak near 1200 cm^{-1}, assigned to C–N stretching in en and C–S/CH_2 backbone modes in edtH_2, undergoes slight shifts upon precursor addition, indicating ligand–metal coordination. These spectral changes support the formation of metal–ligand interactions between the donor atoms in en/edtH_2 and the Ag^+/Bi^{3+} cations, validating the proposed chelation-assisted dissolution mechanism. This process contributes to the formation of a homogeneous molecular precursor solution essential for high-quality thin-film formation.

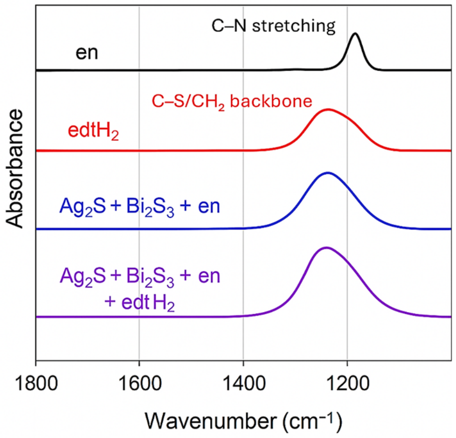

Figure 6. FTIR spectra of en, edtH$_2$, and their mixtures with Ag_2S and Bi_2S_3 in the 1000–1800 cm^{-1} region.

To evaluate the photovoltaic performance of the solution-processed $AgBiS_2$ thin-film, firstly energy band levels of the film were examined to explore the potential HTLs and ETLs to design a proper solar cell device structure. Therefore, ultraviolet photoelectron spectroscopy (UPS) analysis was performed on $AgBiS_2$ thin-film with Ag_2S:Bi_2S_3 molar ratio of 1:1.5. As can be seen in Figure 7c, a maximum valence band (E_{VB}) of 5.6 eV was calculated for the material, then considering the bandgap value of 1.44 eV measured by UV-VIS transmission method, an energy level at 4.16 eV is determined for minimum conduction band (E_{CB}) of the material. Given these, in Figure 7d a range of compounds that can be used as the ELT and HTL with appropriate energy band levels with respect to $AgBiS_2$ to develop a solar cell device structure can be seen. Later on, we explored the developed $AgBiS_2$ thin-films applicability as the light-absorber in device with the planar structure of FTO/c-TiO_2/$AgBiS_2$/P3HT/Au (Figure 7e). J-V curve of the solar cell with best PCE for this structure can be seen in Figure 7f, which shows producing relatively high V_{oc} of 0.397, comparable to those reported earlier [54,75], J_{sc} of 3.89 mA/cm^2, FF of 0.4 and PCE of 0.62%. The incident photon-to-current conversion efficiency (IPCE), which is also known as external quantum efficiency (EQE)), results indicate a relatively broad EQE values from 200 to 900 nm with an integrated photocurrent of 3.71 mA/cm^2 (Figure S8).

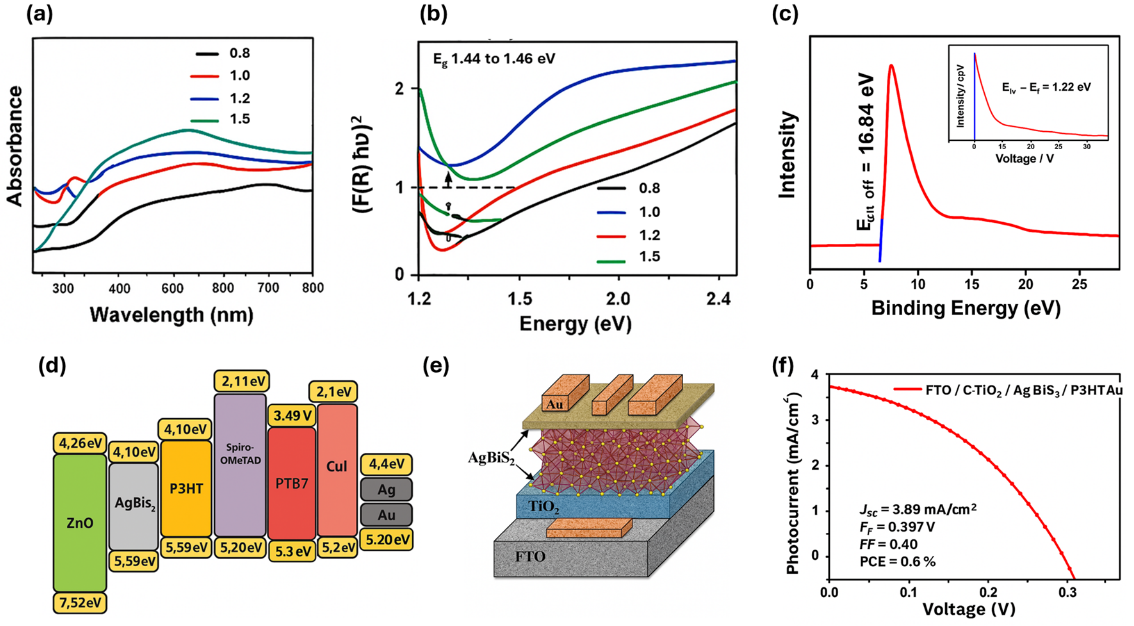

Figure 7. (**a**) Absorption and (**b**) energy bandgap spectrum of $AgBiS_2$ thin-films with different Bi_2S_3/Ag_2S molar ratio using transmission-mode ultraviolet-visible (UV-Vis) measurement. (**c**) Ultraviolet photoemission spectroscopy spectrum of the $AgBiS_2$ film. (**d**) Band alignment of $AgBiS_2$ relative to other ETMs and HTMs. The energy levels of other materials are from other studies. (**e**) Schematic of the solar cell device with the structure of planar FTO/c-TiO_2/$AgBiS_2$/P3HT/Au. (**f**) J-V curve of the best performing devices with $AgBiS_2$ as the active layer.

Theoretically, P3HT with the HOMO level of around 5.59 eV should prepare an acceptable band energy alignment with $AgBiS_2$. However, in the case of the TiO_2, its LUMO value of 4.1 eV may cause some issues to have an efficient photon to current conversion. This can be a reason for low photocurrent density results in our device structure in comparison to the higher ones in the literature using ZnO as the ETL [54,75]. In general ZnO with HUMO level of 4.26 eV as well as its relatively higher electron mobility than TiO_2 should be a more appropriate ETL for the $AgBiS_2$ device structure. Exploring other options of HTLs such as PTB7 (HOMO level of 5.3 eV) [76] or the commonly used spiro-OMeTAD (HOMO level of 5.2 eV) can be a good way to further improve photovoltaic parameters of the presented $AgBiS_2$ solar cell in this work. Another worth-mentioning point is that in the structure proposed by Bernechea et. al [54] and Pai et al. [75], one strategy to improve the performance of the device was modifying the surface of the HTL with MoO_3, which should have an influence on electronic properties of the HTL. While the obtained PCE of 0.62% is modest, it is comparable to early-stage solution-processed $AgBiS_2$ solar cells reported in the literature. For instance, devices fabricated using nanocrystal inks with in situ ligand exchange have shown PCEs around 0.5–1.1%, often requiring complex multi-step synthesis and passivation strategies [54,55]. In our work, the relatively low PCE can be attributed to factors such as suboptimal interface energetics, limited carrier mobility in the current device architecture (FTO/c-TiO_2/$AgBiS_2$/P3HT/Au), and the absence of surface passivation or doping. Future improvements may be achieved by exploring alternative electron transport layers (e.g., ZnO or SnO_2), employing high-mobility hole transport materials, or incorporating interface engineering (e.g., MoO_3 or ultrathin buffer layers) to enhance charge extraction and reduce recombination losses.

Since poor stability of Pb-based perovskites in humidity is one of the obstacles toward their market acceptance, the stability of this device contains $AgBiS_2$ was investigated by storing it in ambient conditions with humidity of 58 ± 4% for 50 days. The changes in photovoltaic parameters of the examined device can be seen in Figure 8a. This initial stability test confirms the strong sustainability of the device against humidity, as it preserves over 98% of its original PCE. Likewise, testing behaviour of bare $AgBiS_2$ thin-film in the humidity of 61 ± 5% yielded to excellent stability of the material in the air for 53 days, as tracing XRD of the material shows no sign of degradation (Figure 8b).

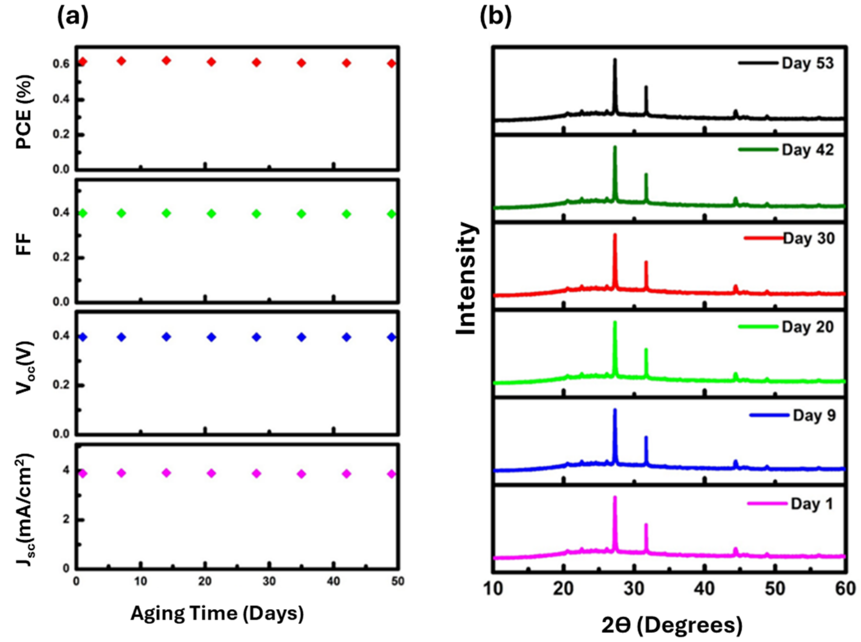

Figure 8. (**a**) Changes in Photovoltaic parameters of solar cells with the structure of FTO/c-TiO_2/$AgBiS_2$/P3HT/Au after storage in air with humidity of 58 ± 4% for 50 days. (**b**) XRD spectra of $AgBiS_2$ thin-film after storage in air with humidity of 61 ± 5% for 53 days.

4. Discussions

Developing a solution-processed deposition method for $AgBiS_2$ thin-films represents a significant advancement toward their integration into optoelectronic applications, particularly photovoltaics. The choice of 1,2-ethylenediamine (en) and 1,2-ethanedithiol ($edtH_2$) as a binary solvent system proved effective in dissolving Ag_2S and Bi_2S_3 precursors, enabling the fabrication of high-quality thin-films. Film morphology and coverage were highly sensitive to the en:$edtH_2$ volume ratio, where a 4:1 ratio produced optimal film quality, avoiding excessive viscosity that hindered uniform deposition. In addition to affecting coverage and smoothness, the en:edtH_2 ratio also appeared to influence grain growth during the annealing process. As seen in Figure 1a–c, increasing the edtH_2 content led to inhomogeneous film spreading, which disrupted uniform nucleation and grain coalescence. In contrast, the optimal 4:1 ratio yielded compact films with improved grain connectivity. These morphological differences suggest that the coordination strength and viscosity of the solvent system not only govern precursor solubility but also indirectly impact crystallisation dynamics and final grain structure. Further optimization revealed that the Ag_2S:Bi_2S_3 precursor molar ratio played a more dominant role than the solvent ratio in determining film compactness, crystallinity, and coverage quality. Specifically, a 1:1.5 molar ratio resulted in a mirror-like film with enhanced uniformity and minimal defects, as confirmed by SEM and AFM analyses. Increasing Bi_2S_3 content not only improved thin-film surface smoothness but also lowered the crystallization temperature to 180 °C, demonstrating a synergistic effect on phase stability.

The solvent system played a pivotal role in enabling the solution processing of $AgBiS_2$ thin-films, owing to its ability to act as a strong chelating medium. The combination of 1,2-ethylenediamine (en) and 1,2-ethanedithiol (edtH_2) effectively dissolves the otherwise insoluble Ag_2S and Bi_2S_3 precursors, facilitating the formation of homogeneous molecular solutions. This enhanced solubility is attributed to the bidentate chelation capability of en and edtH_2, whose amine (–NH_2) and thiol (–SH) functional groups coordinate with Ag^+ and Bi^{3+} cations at multiple binding sites. While the –SH vibrational signature lies outside the measured IR range, coordination-induced shifts in adjacent C–S and CH_2 modes serve as spectral indicators of thiol–metal interactions. This chelation disrupts the metal sulfide lattice through the formation of stable metal–ligand complexes, promoting ionization and stabilizing thiolatochalcogenometallate species in solution [65]. The coordination-assisted dissolution mechanism was experimentally supported by FTIR spectroscopy, which revealed distinct shifts in the 1000–1300 cm^{-1} region. A dominant peak near 1200 cm^{-1}, attributed to C–N stretching in en and C–S/CH_2 modes in edtH_2, undergoes downshifting and broadening upon precursor addition. These spectral changes provide compelling evidence consistent with ligand–metal interactions and support the proposed chelation-assisted dissolution mechanism.

Unlike conventional solvents such as hydrazine-effective but highly toxic-the en:edtH_2 system offers a safer, scalable, and more controllable processing route. The strong chelating environment, supported by spectroscopic and conductivity data, ensures complete dissolution of the precursors and avoids colloidal instability. This facilitates uniform film formation with improved phase purity and compactness. These advantages are directly reflected in the high-quality $AgBiS_2$ thin-films achieved in this study, as confirmed by SEM, AFM, and XRD analyses.

Optoelectronic characterization revealed a progressive enhancement in absorption with increasing Bi_2S_3 content, while the bandgap remained consistent (1.44–1.46 eV), confirming that film quality improvements were primarily morphological rather than band structure modifications. XRD analysis further established that fine-tuning the precursor ratio led to improved phase purity and enhanced crystallinity, eliminating secondary phases at lower annealing temperatures. The fabricated planar heterojunction solar cell (FTO/c-TiO_2/$AgBiS_2$/P3HT/Au) exhibited an initial power conversion efficiency (PCE) of 0.62%, indicating the potential of $AgBiS_2$ thin-films as a light absorber. However, the relatively low short-circuit current density (Jsc) and fill factor (FF) suggest that further improvements are required, particularly in electron transport layer (ETL) selection and surface passivation strategies. Given that previous studies employed ZnO as an ETL, which provides superior electron mobility compared to TiO_2, alternative ETL materials could enhance charge extraction efficiency. Additionally, employing HTLs such as PTB7 or spiro-OMeTAD and incorporating MoO_3 surface modifications, as demonstrated in previous high-efficiency $AgBiS_2$ solar cells [55], may further improve device performance.

A key advantage of $AgBiS_2$ over conventional Pb-based perovskites is its remarkable environmental stability. The solar cell retained 98% of its initial efficiency after 50 days in ambient conditions (humidity ~58%), while bare $AgBiS_2$ thin-films remained structurally intact for over 53 days, as confirmed by XRD. These results highlight $AgBiS_2$ as a highly stable and promising alternative for next-generation photovoltaics. This study demonstrates that precise optimization of precursor composition and deposition conditions enables the fabrication of high-quality, stable $AgBiS_2$ thin-films via a solution-processed spin-coating method. Future work should focus on further understanding the crystallization mechanism in this solvent system, optimizing charge transport layers, and exploring alternative scalable deposition methods to further enhance the performance and commercial viability of $AgBiS_2$ thin-films.

5. Conclusions

In summary, this work presents a feasible solution-processed approach for depositing high-quality $AgBiS_2$ thin-films by dissolving Ag_2S and Bi_2S_3 precursors in a binary solvent system composed of 1,2-ethylenediamine (en) and 1,2-ethanedithiol ($edtH_2$). To optimize film quality, we systematically investigated two key parameters: the en:$edtH_2$ solvent volume ratio and the Ag_2S:Bi_2S_3 precursor molar ratio. The results indicate that the precursor molar ratio has a significant impact on film morphology, with the highest-quality mirror-like $AgBiS_2$ thin-films achieved at an Ag_2S:Bi_2S_3 ratio of 1:1.5. Beyond film coverage, increasing Bi_2S_3 content in the precursor solution facilitated the formation of high-purity cubic-phase $AgBiS_2$ at a lower crystallization temperature of 180 °C, whereas at an Ag_2S:Bi_2S_3 ratio of 1:1, a higher temperature of 210 °C was required. EDS characterization confirmed that the elemental composition of the films closely matched the theoretical stoichiometry, while surface composition analysis indicated that the binding energy values of Ag and Bi aligned with those expected for Ag_2S and Bi_2S_3, verifying the correct phase formation. Optoelectronic analysis revealed a progressive enhancement in absorption with increasing Bi_2S_3 content (Ag_2S:Bi_2S_3 ratio from 1:0.8 to 1:5), while the bandgap remained consistently within the range of 1.44 eV to 1.46 eV. Utilizing this simple, scalable solution-processed deposition method, a planar heterojunction solar cell with the structure FTO/c-TiO_2/$AgBiS_2$/P3HT/Au was fabricated to evaluate the potential of $AgBiS_2$ as a light-absorbing layer for photovoltaic applications. The initial power conversion efficiency (PCE) of 0.62% demonstrates the promise of this material for solar energy harvesting. Furthermore, both the $AgBiS_2$ thin-film and the photovoltaic device exhibited exceptional ambient stability, maintaining structural and operational integrity for approximately 50 days, highlighting the potential of $AgBiS_2$ as a stable and environmentally friendly alternative to Pb-based perovskites.

Supplementary Materials

The additional data and information can be downloaded at: https://media.sciltp.com/articles/others/2505091438463234/MatSus-771-Supplementary-Materials.pdf

Author Contributions

M.G.: conceptualization, methodology, investigation, data curation, writing, original draft preparation, visualization; D.H.: formal analysis, validation, writing, reviewing and editing; B.J.: supervision, project administration, resources, writing, reviewing and editing; X.W.: supervision, funding acquisition, writing, reviewing and editing. All authors have read and agreed to the published version of the manuscript.

Funding

The research leading to these results was financially supported through Discovery, Laureate Fellowship and Linkage programs by the Australian Research Council. Authors also acknowledges the financial support from Australian Research Council (DP220100603, CE230100006, LP240100504 and LE250100078) and from Australian Renewable Energy Agency (ARENA, TM021).

Data Availability Statement

The data presented in this study are available from the corresponding author upon reasonable request. The authors are committed to preserving access to the data for at least 10 years following publication, in accordance with journal policy.

Acknowledgments

The research leading to these results was financially supported through Discovery, Laureate Fellowship and Linkage programs by the Australian Research Council. This work was performed in part at the Queensland node of the Australian National Fabrication Facility, a company established under the National Collaborative Research Infrastructure Strategy to provide nano- and micro-fabrication facilities for Australia’s researchers. The support from the Australian Microscopy & Microanalysis Research Facility at the Centre for Microscopy and Microanalysis, The University of Queensland (UQ) and UQI scholarship are also acknowledged. This work used the RMIT Micro Nano Research Facility (MNRF) in the Victorian Node of the NCRIS-enabled Australian National Fabrication Facility (ANFF-Vic).

Conflicts of Interest

The authors declare no conflict of interest.

References

1. Sharif, R.; Khalid, A.; Ahmad, S.W.; et al. A comprehensive review of the current progresses and material advances in perovskite solar cells. *Nanoscale Adv.* **2023**, *5*, 3803–3833. https://doi.org/10.1039/D3NA00319A.
2. Cao, F.; Bian, L.; Li, L. Perovskite solar cells with high-efficiency exceeding 25%: A review. *Energy Mater. Devices* **2024**, *2*, 9370018. https://doi.org/10.26599/EMD.2024.9370018.
3. Azhar, M.; Yalcinkaya, Y.; Cuzzupè, D.T.; et al. Perovskite Thin Films Solar Cells: The Gas Quenching Method. *Mater. Sustain.* **2025**, *1*, 5. https://doi.org/10.53941/matsus.2025.100005.
4. D'Innocenzo, V.; Grancini, G.; Alcocer, M.J.; et al. Excitons versus free charges in organo-lead tri-halide perovskites. *Nat. Commun.* **2014**, *5*, 3586.
5. De Wolf, S.; Holovsky, J.; Moon, S.-J.; et al. Organometallic halide perovskites: Sharp optical absorption edge and its relation to photovoltaic performance. *J. Phys. Chem. Lett* **2014**, *5*, 1035–1039.
6. Stranks, S.D.; Eperon, G.E.; Grancini, G.; et al. Electron-hole diffusion lengths exceeding 1 micrometer in an organometal trihalide perovskite absorber. *Science* **2013**, *342*, 341–344.
7. Xing, G.; Mathews, N.; Sun, S.; et al. Long-range balanced electron-and hole-transport lengths in organic-inorganic CH3NH3PbI3. *Science* **2013**, *342*, 344–347.
8. Dong, Q.; Fang, Y.; Shao, Y.; et al. Electron-hole diffusion lengths >175 μm in solution-grown $CH_3NH_3PbI_3$ single crystals. *Science* **2015**, *347*, 967–970.
9. Miyata, A.; Mitioglu, A.; Plochocka, P.; et al. Direct measurement of the exciton binding energy and effective masses for charge carriers in organic–inorganic tri-halide perovskites. *Nat. Phys* **2015**, *11*, 582.
10. Chatterjee, S.; Pal, A.J. Influence of metal substitution on hybrid halide perovskites: Towards lead-free perovskite solar cells. *J. Mater. Chem. A* **2018**, *6*, 3793–3823.
11. Zhu, H.; Fu, Y.; Meng, F.; et al. Lead halide perovskite nanowire lasers with low lasing thresholds and high quality factors. *Nat. Mater.* **2015**, *14*, 636.
12. Tan, Z.-K.; Moghaddam, R.S.; Lai, M.L.; et al. Bright light-emitting diodes based on organometal halide perovskite. *Nat. Nanotechnol.* **2014**, *9*, 687.
13. Wang, R.; Mujahid, M.; Duan, Y.; et al. A review of perovskites solar cell stability. *Adv. Funct. Mater.* **2019**, *29*, 1808843.
14. Jeon, N.J.; Noh, J.H.; Yang, W.S.; et al. Compositional engineering of perovskite materials for high-performance solar cells. *Nature* **2015**, *517*, 476–480. https://doi.org/10.1038/nature14133.
15. Lyu, M.; Yun, J.-H.; Cai, M.; et al. Organic–inorganic bismuth (III)-based material: A lead-free, air-stable and solution-processable light-absorber beyond organolead perovskites. *Nano Res.* **2016**, *9*, 692–702.
16. Slavney, A.H.; Hu, T.; Lindenberg, A.M.; et al. A bismuth-halide double perovskite with long carrier recombination lifetime for photovoltaic applications. *J. Am. Chem. Soc.* **2016**, *138*, 2138–2141.
17. Ghasemi, M.; Hao, M.; Xiao, M.; et al. Lead-free metal-halide double perovskites: From optoelectronic properties to applications. *Nanophotonics* **2020**, *10*, 2181–2219. https://doi.org/10.1515/nanoph-2020-0548.
18. Flora, G.; Gupta, D.; Tiwari, A. Toxicity of lead: A review with recent updates. *Interdiscip. Toxicol.* **2012**, *5*, 47–58.
19. Billen, P.; Leccisi, E.; Dastidar, S.; et al. Comparative evaluation of lead emissions and toxicity potential in the life cycle of lead halide perovskite photovoltaics. *Energy* **2019**, *166*, 1089–1096. https://doi.org/10.1016/j.energy.2018.10.141.
20. Hao, F.; Stoumpos, C.C.; Guo, P.; et al. Solvent-mediated crystallization of CH3NH3SnI$_3$ films for heterojunction depleted perovskite solar cells. *J. Am. Chem. Soc.* **2015**, *137*, 11445–11452.
21. Fujihara, T.; Terakawa, S.; Matsushima, T.; et al. Fabrication of high coverage $MASnI_3$ perovskite films for stable, planar heterojunction solar cells. *J. Mater. Chem. C* **2017**, *5*, 1121–1127.
22. Yokoyama, T.; Cao, D.H.; Stoumpos, C.C.; et al. Overcoming short-circuit in lead-free $CH_3NH_3SnI_3$ perovskite solar cells via kinetically controlled gas–solid reaction film fabrication process. *J. Phys. Chem. Lett* **2016**, *7*, 776–782.
23. Noel, N.K.; Stranks, S.D.; Abate, A.; et al. Lead-free organic–inorganic tin halide perovskites for photovoltaic applications. *Energy Environ. Sci.* **2014**, *7*, 3061–3068.
24. Cui, X.-P.; Jiang, K.-J.; Huang, J.-H.; et al. Cupric bromide hybrid perovskite heterojunction solar cells. *Synth. Met.* **2015**, *209*, 247–250.
25. Wei, F.; Deng, Z.; Sun, S.; et al. The synthesis, structure and electronic properties of a lead-free hybrid inorganic–organic double perovskite (MA) 2 KBiCl 6 (MA = methylammonium). *Mater. Horiz.* **2016**, *3*, 328–332.
26. Li, X.; Zhong, X.; Hu, Y.; et al. Organic–Inorganic Copper (II)-Based Material: A Low-Toxic, Highly Stable Light Absorber for Photovoltaic Application. *J. Phys. Chem. Lett* **2017**, *8*, 1804–1809.
27. Zhu, H.; Pan, M.; Johansson, M.B.; et al. High Photon-to-Current Conversion in Solar Cells Based on Light-Absorbing Silver Bismuth Iodide. *ChemSusChem* **2017**, *10*, 2592–2596.
28. Eckhardt, K.; Bon, V.; Getzschmann, J.; et al. Crystallographic insights into $(CH_3NH_3)_3(Bi_2I_9)$: A new lead-free hybrid organic–inorganic material as a potential absorber for photovoltaics. *Chem. Commun.* **2016**, *52*, 3058–3060.

29. Fabian, D.M.; Ardo, S. Hybrid organic–inorganic solar cells based on bismuth iodide and 1,6-hexanediammonium dication. *J. Mater. Chem. A* **2016**, *4*, 6837–6841.
30. Hoye, R.L.; Brandt, R.E.; Osherov, A.; et al. Methylammonium bismuth iodide as a lead-free, stable hybrid organic–inorganic solar absorber. *Chem. Eur. J.* **2016**, *22*, 2605–2610.
31. Ghasemi, M.; Lyu, M.; Roknuzzaman, M.; et al. Phenethylammonium bismuth halides: From single crystals to bulky-organic cation promoted thin-film deposition for potential optoelectronic applications. *J. Mater. Chem. A* **2019**, *7*, 20733–20741. https://doi.org/10.1039/C9TA07454F.
32. Ghasemi, M.; Zhang, L.; Yun, J.-H.; et al. Dual-Ion-Diffusion Induced Degradation in Lead-Free $Cs_2AgBiBr_6$ Double Perovskite Solar Cells. *Adv. Funct. Mater.* **2020**, *30*, 2002342. https://doi.org/10.1002/adfm.202002342.
33. Boopathi, K.M.; Karuppuswamy, P.; Singh, A.; et al. Solution-processable antimony-based light-absorbing materials beyond lead halide perovskites. *J. Mater. Chem. A* **2017**, *5*, 20843–20850.
34. Saparov, B.; Hong, F.; Sun, J.-P.; et al. Thin-film preparation and characterization of $Cs_3Sb_2I_9$: A lead-free layered perovskite semiconductor. *Chem. Mater.* **2015**, *27*, 5622–5632.
35. Harikesh, P.; Mulmudi, H.K.; Ghosh, B.; et al. Rb as an alternative cation for templating inorganic lead-free perovskites for solution processed photovoltaics. *Chem. Mater.* **2016**, *28*, 7496–7504.
36. Bator, G.; Jakubas, R.; Baran, J.; et al. Infrared studies of structural phase transitions in $(NH_3CH_3)_3Sb_2I_9$. *Vib. Spectrosc.* **1995**, *8*, 425–433.
37. Krishnamoorthy, T.; Ding, H.; Yan, C.; et al. Lead-free germanium iodide perovskite materials for photovoltaic applications. *J. Mater. Chem. A* **2015**, *3*, 23829–23832.
38. Stoumpos, C.C.; Frazer, L.; Clark, D.J.; et al. Hybrid germanium iodide perovskite semiconductors: Active lone pairs, structural distortions, direct and indirect energy gaps, and strong nonlinear optical properties. *J. Am. Chem. Soc.* **2015**, *137*, 6804–6819.
39. Lu, X.; Zhao, Z.; Li, K.; et al. First-principles insight into the photoelectronic properties of Ge-based perovskites. *RSC Adv.* **2016**, *6*, 86976–86981.
40. Lakshmi, V.; Chen, Y.; Mikhaylov, A.A.; et al. Nanocrystalline SnS_2 coated onto reduced graphene oxide: Demonstrating the feasibility of a non-graphitic anode with sulfide chemistry for potassium-ion batteries. *Chem. Commun.* **2017**, *53*, 8272–8275.
41. Gao, M.-R.; Xu, Y.-F.; Jiang, J.; et al. Nanostructured metal chalcogenides: Synthesis, modification, and applications in energy conversion and storage devices. *Chem. Soc. Rev.* **2013**, *42*, 2986–3017.
42. Anantharaj, S.; Ede, S.R.; Sakthikumar, K.; et al. Recent trends and perspectives in electrochemical water splitting with an emphasis on sulfide, selenide, and phosphide catalysts of Fe, Co, and Ni: A review. *ACS Catal* **2016**, *6*, 8069–8097.
43. Chatti, M.; Gengenbach, T.; King, R.; et al. Vertically aligned interlayer expanded MoS_2 nanosheets on a carbon support for hydrogen evolution electrocatalysis. *Chem. Mater.* **2017**, *29*, 3092–3099.
44. Chung, I.; Kanatzidis, M.G. Metal chalcogenides: A rich source of nonlinear optical materials. *Chem. Mater.* **2013**, *26*, 849–869.
45. Fan, F.-J.; Wu, L.; Yu, S.-H. Energetic I–III–VI 2 and I 2–II–IV–VI 4 nanocrystals: Synthesis, photovoltaic and thermoelectric applications. *Energy Environ. Sci.* **2014**, *7*, 190–208.
46. Carey, G.H.; Abdelhady, A.L.; Ning, Z.; et al. Colloidal quantum dot solar cells. *Chem. Rev.* **2015**, *115*, 12732–12763.
47. Panthani, M.G.; Kurley, J.M.; Crisp, R.W.; et al. High efficiency solution processed sintered CdTe nanocrystal solar cells: The role of interfaces. *Nano Lett.* **2014**, *14*, 670–675.
48. Chen, G.; Seo, J.; Yang, C.; et al. Nanochemistry and nanomaterials for photovoltaics. *Chem. Soc. Rev.* **2013**, *42*, 8304–8338.
49. Aldakov, D.; Lefrançois, A.; Reiss, P. Ternary and quaternary metal chalcogenide nanocrystals: Synthesis, properties and applications. *J. Mater. Chem. C* **2013**, *1*, 3756–3776.
50. Yan, C.; Gu, E.; Liu, F.; et al. Colloidal synthesis and characterizations of wittichenite copper bismuth sulphide nanocrystals. *Nanoscale* **2013**, *5*, 1789–1792.
51. Guin, S.N.; Biswas, K. Cation disorder and bond anharmonicity optimize the thermoelectric properties in kinetically stabilized rocksalt AgBiS2 nanocrystals. *Chem. Mater.* **2013**, *25*, 3225–3231.
52. Chen, C.; Qiu, X.; Ji, S.; et al. The synthesis of monodispersed AgBiS 2 quantum dots with a giant dielectric constant. *CrystEngComm* **2013**, *15*, 7644–7648.
53. Pejova, B.; Nesheva, D.; Aneva, Z.; et al. Photoconductivity and relaxation dynamics in sonochemically synthesized assemblies of $AgBiS_2$ quantum dots. *J. Phys. Chem. C* **2010**, *115*, 37–46.
54. Bernechea, M.; Miller, N.C.; Xercavins, G.; et al. Solution-processed solar cells based on environmentally friendly $AgBiS_2$ nanocrystals. *Nat. Photonics* **2016**, *10*, 521.
55. Oh, J.T.; Wang, Y.; Rodà, C.; et al. Post-deposition in situ passivation of $AgBiS_2$ nanocrystal inks for high-efficiency ultra-thin solar cells. *Energy Environ. Sci.* **2024**, *17*, 8885–8892.

56. Nakazawa, T.; Kim, D.; Oshima, Y.; et al. Synthesis and Application of $AgBiS_2$ and Ag_2S Nanoinks for the Production of IR Photodetectors. *ACS Omega* **2021**, *6*, 20710–20718. https://doi.org/10.1021/acsomega.1c03463.
57. Ajiboye, T.O.; Mafolasire, A.A.; Lawrence, S.; et al. Composite and Pristine Silver Bismuth Sulphide: Synthesis and Up-to-Date Applications. *J. Inorg. Organomet. Polym. Mater.* **2024**, *34*, 433–457. https://doi.org/10.1007/s10904-023-02838-y.
58. Guan, W.; Zhou, W.; Lu, J.; et al. Luminescent films for chemo-and biosensing. *Chem. Soc. Rev.* **2015**, *44*, 6981–7009.
59. Kim, D.; Jeong, Y.; Song, K.; et al. Inkjet-printed zinc tin oxide thin-film transistor. *Langmuir* **2009**, *25*, 11149–11154.
60. Meyers, S.T.; Anderson, J.T.; Hung, C.M.; et al. Aqueous inorganic inks for low-temperature fabrication of ZnO TFTs. *J. Am. Chem. Soc.* **2008**, *130*, 17603–17609.
61. Mitzi, D.B.; Yuan, M.; Liu, W.; et al. A high-efficiency solution-deposited thin-film photovoltaic device. *Adv. Mater.* **2008**, *20*, 3657–3662.
62. Bob, B.; Lei, B.; Chung, C.H.; et al. The Development of Hydrazine-Processed Cu (In, Ga)(Se, S)$_2$ Solar Cells. *Adv. Energy Mater.* **2012**, *2*, 504–522.
63. Wang, R.Y.; Caldwell, M.A.; Jeyasingh, R.G.D.; et al. Electronic and optical switching of solution-phase deposited SnSe2 phase change memory material. *J. Appl. Phys.* **2011**, *109*, 113506.
64. Milliron, D.J.; Raoux, S.; Shelby, R.M.; et al. Solution-phase deposition and nanopatterning of GeSbSe phase-change materials. *Nat. Mater.* **2007**, *6*, 352.
65. Webber, D.H.; Brutchey, R.L. Alkahest for V2VI3 chalcogenides: Dissolution of nine bulk semiconductors in a diamine-dithiol solvent mixture. *J. Am. Chem. Soc.* **2013**, *135*, 15722–15725.
66. Banerjee, S.; Szarko, J.M.; Yuhas, B.D.; et al. Room temperature light emission from the low-dimensional semiconductors $AZrPS_6$ (A = K, Rb, Cs). *J. Am. Chem. Soc.* **2010**, *132*, 5348–5350.
67. Norian, K.; Chern, G.; Lauks, I. Morphology and thermal properties of solvent-cast arsenic sulfide films. *J. Appl. Phys.* **1984**, *55*, 3795–3798.
68. Bera, T.K.; Jang, J.I.; Song, J.-H.; et al. Soluble semiconductors $AAsSe_2$ (A = Li, Na) with a direct-band-gap and strong second harmonic generation: A combined experimental and theoretical study. *J. Am. Chem. Soc.* **2010**, *132*, 3484–3495.
69. Mitzi, D.B. Solution processing of chalcogenide semiconductors via dimensional reduction. *Adv. Mater.* **2009**, *21*, 3141–3158.
70. Yuan, M.; Mitzi, D.B. Solvent properties of hydrazine in the preparation of metal chalcogenide bulk materials and films. *Dalton Trans.* **2009**, *31*, 6078–6088.
71. Guo, Q.; Ford, G.M.; Yang, W.-C.; et al. Fabrication of 7.2% efficient CZTSSe solar cells using CZTS nanocrystals. *J. Am. Chem. Soc.* **2010**, *132*, 17384–17386.
72. Wang, W.; Gao, C.; Chen, Y.; et al. Cubic $AgBiS_2$ Powder Prepared Using a Facile Reflux Method for Photocatalytic Degradation of Dyes. *Micromachines* **2023**, *14*, 2211.
73. Sugarthi, S.; Bakiyaraj, G.; Abinaya, R.; et al. Effect of different growth temperature on the formation of ternary metal chalcogenides $AgBiS_2$. *Mater. Sci. Semicond. Process.* **2020**, *107*, 104781.
74. Yao, F.; Jiang, L.; Qi, Y.; et al. Chemical bath deposition of $AgBiS_2$ films for visible and X-ray detection. *Appl. Mater. Today* **2022**, *26*, 101262.
75. Pai, N.; Lu, J.; Senevirathna, D.C.; et al. Spray deposition of $AgBiS_2$ and Cu_3 BiS_3 thin films for photovoltaic applications. *J. Mater. Chem. C* **2018**, *6*, 2483–2494.
76. Cappel, U.B.; Daeneke, T.; Bach, U. Oxygen-induced doping of spiro-MeOTAD in solid-state dye-sensitized solar cells and its impact on device performance. *Nano Lett.* **2012**, *12*, 4925–4931.